Registration of phase-contrast images in propagation-based X-ray phase tomography

L. WEBER*,†,‡, A. HÄNSCH*, U. WOLFRAM§, A. PACUREANU†, P. CLOETENS†, F. PEYRIN*,†, S. RIT* & M. LANGER* ID

*Univ. Lyon, INSA-Lyon, Université Claude Bernard Lyon 1, CNRS UMR 5220, Inserm U1206, CREATIS, Lyon, France

†ESRF, The European Synchrotron, Grenoble, France

‡Currently at Centre Jean Perrin, Service de Physique Médicale, Clermont-Ferrand, France

§School of Engineering and Physical Sciences (EPS), Institute of Mechanical, Process and Energy Engineering (IMPEE), Heriot-Watt University, Edinburgh, UK

Summary

X-ray phase tomography aims at reconstructing the 3D electron density distribution of an object. It offers enhanced sensitivity compared to attenuation-based X-ray absorption tomography. In propagation-based methods, phase contrast is achieved by letting the beam propagate after interaction with the object. The phase shift is then retrieved at each projection angle, and subsequently used in tomographic reconstruction to obtain the refractive index decrement distribution, which is proportional to the electron density. Accurate phase retrieval is achieved by combining images at different propagation distances. For reconstructions of good quality, the phase-contrast images recorded at different distances need to be accurately aligned. In this work, we characterise the artefacts related to misalignment of the phase-contrast images, and investigate the use of different registration algorithms for aligning inline phase-contrast images. The characterisation of artefacts is done by a simulation study and comparison with experimental data. Loss in resolution due to vibrations is found to be comparable to attenuation-based computed tomography. Further, it is shown that registration of phase-contrast images is nontrivial due to the difference in contrast between the different images, and the often periodical artefacts present in the phase-contrast images if multilayer X-ray optics are used. To address this, we compared two registration algorithms for aligning phase-contrast images acquired by magnified X-ray nanotomography: one based on cross-correlation and one based on mutual information. We found that the mutual information-based registration algorithm was more robust than a correlation-based method.

L. Weber and A. Hänsch contributed equally.

Correspondence to: M. Langer, Univ. Lyon, INSA-Lyon, Université Claude Bernard Lyon 1, CNRS UMR 5220, Inserm U1206, CREATIS, 69621 Lyon, France. Tel: +33472438258; e-mail: max.langer@esrf.fr

Introduction

X-ray phase-contrast microcomputed tomography (μCT) is a relatively new imaging modality, which offers several advantages for the investigation of biological samples, compared to standard attenuation μCT (Boistel *et al.*, 2011; Zanette *et al.*, 2011). Phase-contrast μCT has been shown to be several orders of magnitude more sensitive than standard μCT (Momose & Fukuda, 1995), particularly in the hard X-ray domain. This is especially interesting for the imaging of structures in soft tissue (Guigay *et al.*, 2007; Horng *et al.*, 2014). Further, due to the higher sensitivity, the dose absorbed by the sample can be kept lower than with attenuation-based techniques. As opposed to attenuation, the phase of an X-ray beam cannot be measured directly, however. Several ways to achieve contrast from the phase of the X-ray beam have been invented (Zanette *et al.*, 2013). In this work, we only consider free space propagation, known in the literature variously as Fresnel diffraction, in-line holography, and propagation-based imaging (PBI).

PBI is implemented by letting a highly coherent X-ray beam propagate in free space after interaction with an object, before measuring with an X-ray imaging detector (Snigirev *et al.*, 1995). The resulting Fresnel diffraction patterns, or phase-contrast images, can be used directly as input to a tomographic reconstruction algorithm, where it yields an edge enhancement effect. This is due to the phase contrast being sensitive approximately to the Laplacian of the phase of the wave-field. The resulting modality is called phase-contrast tomography (Cloetens *et al.*, 1997). Although this can be an interesting modality in its own right, the nonlinear quantitative relationship between phase shift and contrast can be used to reconstruct the phase shift. This inverse problem is called phase retrieval. Once the phase is retrieved, it can be used to reconstruct the 3D refractive index decrement distribution in the object. This imaging modality is called phase tomography

(Cloetens *et al.*, 1999; Herman, 2009; Langer *et al.*, 2014). It has the advantage over phase-contrast tomography of yielding a contrast that is proportional to the electron density (i.e. mass density for most materials) distribution, rather than edge contrast related to the second derivative of the refractive index decrement distribution.

Several algorithms for phase retrieval from Fresnel diffraction patterns have been developed. Most of these rely on linearisation of the Fresnel diffraction model to yield efficient algorithms using linear filtering (Nugent *et al.*, 1996; Cloetens *et al.*, 1999; Guigay *et al.*, 2007). Two approaches commonly used for phase retrieval from Fresnel diffraction patterns are the Transport of Intensity Equation (TIE) (Teague, 1982; Nugent *et al.*, 1996; Paganin *et al.*, 2002) and the Contrast Transfer Function (CTF) (Guigay, 1977; Cloetens *et al.*, 1999). The TIE is valid for short object-to-detector distances and the CTF is valid for objects with slowly varying phase and weak absorption.

Information transfer from phase shift to contrast in the low spatial frequency range is weak, which makes phase retrieval from Fresnel diffraction patterns sensitive to low-frequency noise (Langer *et al.*, 2010). Several approaches to overcome this limitation have been proposed. Paganin *et al.* (2002) introduced a homogeneity criterion on the object in the TIE, thus achieving a single distance phase retrieval algorithm (generally, phase retrieval using the TIE requires two acquisition planes, e.g. Gbur & Wolf, 2002). Object homogeneity has also been used in the CTF-based methods, but rather introduced as an *a priori* on the low spatial frequencies of the phase (Langer *et al.*, 2010). This approach has been extended to multimaterial (Langer *et al.*, 2012a,b) and heterogeneous objects (Langer *et al.*, 2014) under the assumption that the sample composition is roughly known.

One particularity of the CTF-based methods is that they allow the use of several phase-contrast images taken at different sample-to-detector distances. This allows for a better coverage of the recorded phase information in the frequency domain (Zabler *et al.*, 2005), at the cost of increased acquisition time (notably camera displacement and extra reference images; the exposure time is not necessarily increased (Frachon *et al.*, 2015)) and computational load (image registration of the phase-contrast images taken at different distances). Using several distances seems necessary to achieve good image quality in high-resolution imaging (Langer *et al.*, 2012a,b). A similar problem exists in high-resolution transmission electron microscopy, which is known as a through focal series reconstruction (Op de Beeck *et al.*, 1996).

In these techniques however, the diffraction patterns at different distances need to be aligned. They can be out of alignment due to instrumental imprecisions, drift and vibrations. This problem has been mentioned only briefly in literature despite being nontrivial, especially at high resolution. Specifically, this is a registration problem where the images are similar but not identical, due to the different propagation

distances. At lower resolution the contrast is reasonably similar in the images recorded at different distances, whereas at higher resolution the contrast can be very different at the different distances. Usually, this registration problem is handled using correlation-based methods. In our experience, these approaches work well at relatively low resolutions and in the absence of strong artefacts (especially periodic artefacts such as stripes from X-ray multilayer monochromator optics), but fail more often as resolutions become higher. One reason may be that the intensity in the images can be quite different, whereas registration based on cross-correlation assumes that the intensities do not change, only the position of the image.

Therefore, the aim of this work is to investigate the impact of this registration step on the image quality in the final reconstructed phase tomography image. First, we conducted a simulation study to investigate qualitatively and quantitatively the impact of different misalignments resulting from different types of instrumental instability. We then compared the simulated artefacts to artefacts present in experimental images acquired at the European Synchrotron Radiation Facility (ESRF, Grenoble, France). Finally, we investigated the use of different registration methods, one based on cross-correlation and one based on mutual information, for the alignment of Fresnel diffraction patterns acquired at different distances. Applied to experimental data, the mutual information-based method was found to be more robust to the type of artefacts encountered in practice.

Materials and methods

Image formation

The experimental set-up of free-space propagation-based tomography is described in Figure 1. The data simulation is based on the assumption that an object can be fully described by its complex refractive index distribution

$$n(x, y, z) = 1 - \delta_n(x, y, z) + i\beta(x, y, z), \tag{1}$$

where β is the attenuation index and δ_n is the refractive index decrement, which is related to the phase shift that is induced on the incident wave front $u_{inc}(\mathbf{x})$ with $\mathbf{x} = (x, y)$. For X-rays, the real part of n is very close to, but always smaller than, 1 and is therefore usually written as $1 - \delta_n$. Here, z describes the propagation direction and $\mathbf{x} = (x, y)$ are the coordinates of the plane perpendicular to the propagation direction.

At each projection angle θ and distance D, the intensity $I_{\theta,D}(\mathbf{x})$ is measured. It denotes the intensity of the wave $u_{\theta,D}(\mathbf{x})$ after interaction with the object, which is known as an in-line phase-contrast image or Fresnel diffraction pattern. This can be written as

$$I_{\theta,D}(\mathbf{x}) = |u_{\theta,D}(\mathbf{x})|^2. \tag{2}$$

The wave front $u_{\theta,0}(\mathbf{x})$ at propagation distance zero, that is, at the exit plane of the object, can be modelled by the

multiplication of the incident wave front $u_{inc}(\mathbf{x})$ with the transmittance function of the object

$$T_\theta(\mathbf{x}) = \exp\left[-B_\theta(\mathbf{x}) + i\varphi_\theta(\mathbf{x})\right] \qquad (3)$$

so that

$$u_{\theta,0}(\mathbf{x}) = T_\theta(\mathbf{x})u_{inc}(\mathbf{x}). \qquad (4)$$

Usually a flat illumination is assumed, for simplicity, in which case $u_{inc}(\mathbf{x})$ can be dropped. By assuming a thin object, that is scattering and secondary events are disregarded, the attenuation $B(\mathbf{x})$ and the phase shift $\varphi(\mathbf{x})$ can be considered as projections through the absorption and refractive index distributions

$$B(\mathbf{x}) = \frac{2\pi}{\lambda} \int \beta(\mathbf{x}, z)\mathrm{d}z, \qquad (5)$$

$$\varphi(\mathbf{x}) = -\frac{2\pi}{\lambda} \int \delta_n(\mathbf{x}, z)\mathrm{d}z. \qquad (6)$$

Propagation over a relatively small distance D can be modelled as a linear system, that is as a convolution with the Fresnel propagator. For our purposes, it is more convenient to express this convolution as a multiplication in the Fourier domain

$$\tilde{u}_D(\mathbf{f}) = \tilde{P}_D(\mathbf{f})\tilde{u}_0(\mathbf{f}), \qquad (7)$$

where tilde denotes the Fourier transform and $\mathbf{f} = (f_x, f_y)$ are the frequency coordinates conjugate to $\mathbf{x}$. The Fourier transform of the Fresnel propagator is given by (Goodman, 2005)

$$\tilde{P}_D(\mathbf{f}) = \exp(-i\pi\lambda D|\mathbf{f}|^2). \qquad (8)$$

Simulations

Synthetic projection data were generated by simulating the straight line projections in Eqs. (5) and (6) separately, then assembling the resulting wavefield Eq. (3). Propagation was simulated by implementing Eqs. (7) and (8), first taking the FFT of the wavefield $u_{\theta,0}(\mathbf{x})$, multiplying with the Fourier transform of the propagator (Eq. (8)), then taking the inverse FFT. The Fresnel diffraction patterns were then obtained by taking the squared modulus of the propagated wave (Eq. (2)). To avoid aliasing effects, projections and propagation were simulated on a 2048×2048 grid. The diffraction patterns were then binned to 512×512, to emulate the effect of a CCD detector. Simulated data was generated using a sphere and a modified 3D Shepp–Logan phantom (Langer *et al.*, 2008) at four different propagation distances, assuming fully coherent X-rays of wavelength $\lambda = 0.5166\,\text{Å}$, corresponding to an X-ray energy of 24 keV. A total of 712 projection angles were used. Projection data was simulated in a parallel geometry, using RTK (Rit *et al.*, 2014) and analytical definitions of the phantoms and calculation of the projections. Propagation and detection was simulated using GNU Octave.

Motion. Different kinds of motion of the sample that could occur during data acquisition were simulated, with the purpose to show their effect on the retrieved phase maps and reconstructed volumes. Therefore, we implemented the following misalignments:

- a constant shift of all projections in each propagation distance, caused for example by a misalignment of the detector when going from one propagation distance to the next,
- a continuous linear shift of the projections, that is drift of the sample or detector during the measurement,
- a random, normally distributed shift of the projections, introduced to model vibration of the equipment during data acquisition.

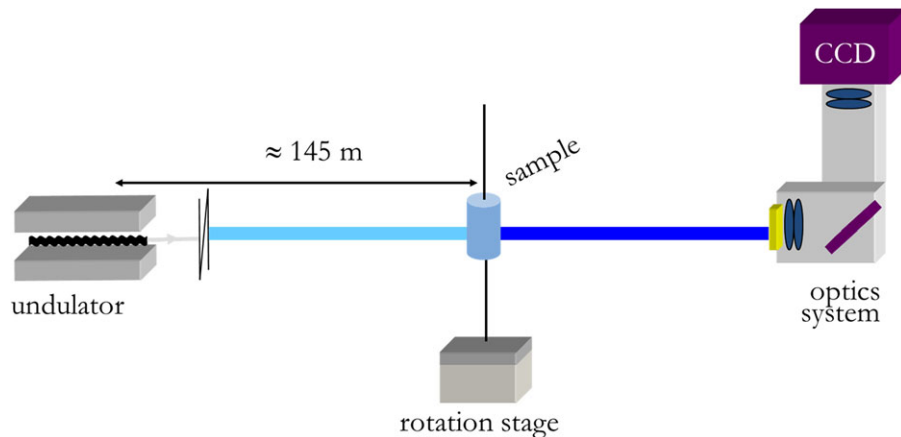All shifts are to be understood as shifts of the propagated projections in the projection plane, that is along the *x*- or

Fig. 1. A typical synchrotron radiation X-ray propagation-based phase-contrast imaging set-up. The sample is mounted on a translation-rotation stage, either directly in the insertion device beam, or in the beam exiting the monochromator optics. The image is recorded on an indirect detection CCD detector.

y-axis, which were introduced in 'Image formation' section, where the y axis physically is the vertical direction and is parallel to the sample axis of rotation. The magnitude and orientation (horizontal, vertical or both) of the chosen motion type was set separately for each propagation distance.

Experimental data

The registration algorithms were evaluated on two different experimental data sets: a constructed wire phantom test object using μCT, and a bone micropillar sample imaged using phase nanotomography.

Wire phantom phase μCT.   A phantom object was constructed for verification purposes. This phantom is composed of a 99.99 % Al wire ($\varnothing$ 125 μm), a bundle of alumina (Al_2O_3) fibres ($\varnothing$ 20 μm), polyethylene terephthalate (PET) monofilaments ($\varnothing$ 200 μm) and polypropylene (PP) fibres ($\varnothing$ 28 μm), fitted inside a Pyrex capillary with 1 mm inner diameter. All materials were acquired from (Goodfellow SARL, Lille, France). The phantom was imaged at the ESRF ID19 beamline using a FReLoN camera with a 2048 × 2048 CCD, a GADOX scintillator and standard microscope optics yielding an effective pixel size of 0.7 μm, with an X-ray energy of 22.5 keV selected by a double Si crystal monochromator. A total of 1500 projections were recorded over a 180° range at four sample-to-detector distances $D = [2, 10, 20, 45]$ mm.

Bone micropillar phase nanotomography.   Bone micropillar samples were prepared at the Institute for Surgical Technology and Biomechanics (ISTB, Bern, Switzerland) and the Swiss Federal Laboratories of Material Science and Technology (EMPA, Thun, Switzerland). A micropillar was sculpted with a combination of ultramilling, high-pulse laser ablation, and focused ion beam (FIB) at the top of a conical compact sheep bone (Schwiedrzik *et al.*, 2014). Image acquisition was made at ID16A beamline (ESRF, Grenoble). The energy of the beam was set to 33.6 keV and focused by Kirkpatrick–Baez optics. The sample was placed behind the focus, creating a divergent beam geometry. Images were recorded using a FReLoN camera with a 2048 × 2048 CCD, a GGG:Eu scintillator and standard microscope optics. The focus to sample distance was 10.525 mm and the sample to detector distance was 1.252 m, yielding an effective pixel size of 25 nm. A total of 2000 projections were acquired over a 180° range, with an exposure time of 0.4 s per projection.

Phase retrieval and tomographic reconstruction

The reconstruction in in-line phase tomography is usually split in two steps. First, the phase is retrieved at each rotation angle. Then, the resulting phase maps are used as input to a tomographic reconstruction algorithm.

Phase retrieval is a nonlinear inverse problem, due to the squared modulus of the complex wave function in Eq. (2). This expression can be linearised, however, in order to yield efficient phase retrieval algorithms. One approach that uses linearisation is called the Contrast Transfer Function (CTF) (Cloetens *et al.*, 1999). The transmittance function (Eq. (3)) is linearised by a Taylor expansion, keeping only the first-order terms (Cloetens *et al.*, 1999; Cloetens *et al.*, 2002):

$$T(\mathbf{x}) \approx 1 - B(\mathbf{x}) + i\varphi(\mathbf{x}). \qquad (8)$$

This linearisation with respect to the amplitude and phase modulation assumes an object with weak absorption and a slowly varying phase (Guigay *et al.*, 2007).

Using a representation of the Fourier Transform of the Fresnel diffraction pattern (Guigay, 1977)

$$\tilde{I}_D(\mathbf{f}) = \int T\left(\mathbf{x} - \frac{\lambda D\mathbf{f}}{2}\right) T^*\left(\mathbf{x} + \frac{\lambda D\mathbf{f}}{2}\right) \exp(-i2\pi\mathbf{x}\cdot\mathbf{f})\, d\mathbf{x}$$

$$(9)$$

and substituting Eq. (8) we have

$$\tilde{I}_D(\mathbf{f}) = \delta_{Dirac}(\mathbf{f}) - 2\cos(\pi\lambda D|\mathbf{f}|^2)\tilde{B}(\mathbf{f}) + 2\sin(\pi\lambda D|\mathbf{f}|^2)\tilde{\varphi}(\mathbf{f}),$$

$$(10)$$

which can be solved for the Fourier transform $\tilde{\varphi}(\mathbf{f})$ of the phase (Cloetens *et al.*, 1999). However, the phase factor in Eq. (10) can have zero-crossings; therefore several propagation distances need to be combined in order to cover the whole frequency domain (Zabler *et al.*, 2005). In addition, the factor $\sin(\pi\lambda D|\mathbf{f}|^2)$ also approaches zero for low frequencies, which can cause low-frequency noise in reconstructions (Langer *et al.*, 2008).

For the simulated data we used the CTF model, a linear least squares approach and Tikhonov regularisation to retrieve the phase from several distances. For the wire phantom, the mixed approach with a homogeneous object prior was used. For the bone micro pillar, a multidistance version of Paganin's method (Paganin *et al.*, 2002; Villanova *et al.*, 2014; Yu *et al.*, submitted) using least-squares, followed by 10 iterations of a nonlinear conjugate gradient algorithm. In all cases, filtered backprojection was used to reconstruct the refractive index decrement distribution of the sample from the retrieved phase maps. We used the PyHST2 hybrid distributed code for high-speed tomographic reconstruction (Mirone *et al.*, 2013).

Registration of phase-contrast images

General scheme.   The first aim of the simulations was to show the resulting artefacts due to misalignments of the phase-contrast images on the retrieved phase maps and tomographic reconstructions. This can be used by the practitioner to determine if an artefact is due to misalignment. In practice however, when imaging real samples, one wants rather to correct any motion of the sample or detector before carrying out the phase

retrieval in order to eliminate as many artefacts from motion as possible. Therefore, several steps for motion correction are carried out before retrieving the phase. The first step consists in a first correction of drift of the sample during the data acquisition. For this purpose, an additional image at a number of projections at specific angles, for example 180°, 90°, and 0° in the case of a 180° scan, is recorded once the tomographic scan is completed. These images are then registered to the projections measured during the scan. The resulting measurements are fitted with a sinusoid, which allows correcting for linear displacements of the sample with respect to the rotation axis during the scan. The propagation distance that had the least movement is chosen as the target distance to which the other distances will be aligned, and the motion correction is applied to this distance. The second step is registration of the phase-contrast images at different propagation distances. For every projection at a certain interval, usually every 100 projections, the vertical and horizontal shifts between two successive projection planes are determined. The shifts for all projection angles are calculated by polynomial interpolation. The degrees of the polynomials are parameters dependent on the smoothness of the motion. Here, we used a sixth- and second-order polynomial in the horizontal and vertical direction respectively, determined empirically. They

are the default values used in practice. The difference in order is due to the motion in the vertical direction being smoother than that in the horizontal. This approach assumes that any motion is smooth, for example due to a continuous drift of the sample. Finally, before phase retrieval, the images at the different distances are aligned to the reference plane image.

Cross-correlation-based method.   Usually, the registration method to determine the shifts was a local search for an optimum of the cross-correlation between the fixed and the moving image. The moving image is translated by shifts that are defined by a given window, usually 5 × 5. Then, for each shift, the distance measure to the fixed image is evaluated. This method assumes that the shifts between two successive planes are small, because large shifts take longer time to calculate. It is also sensitive to local minima. As an example, Figure 2 depicts the shifts for a scan with four propagation distances, where distance 3 is chosen as the reference plane. Hence, distance 2 and 4 are registered to distance 3, and distance 1 is registered to distance 2, the total displacement of distance 1 thus being the sum of the displacement of plane 2 with respect to plane 3 and plane 1 with respect to plane 2. The blue line corresponds to measured shift values, in this case every 100 projections. The red curve is the corresponding polynomial fit.
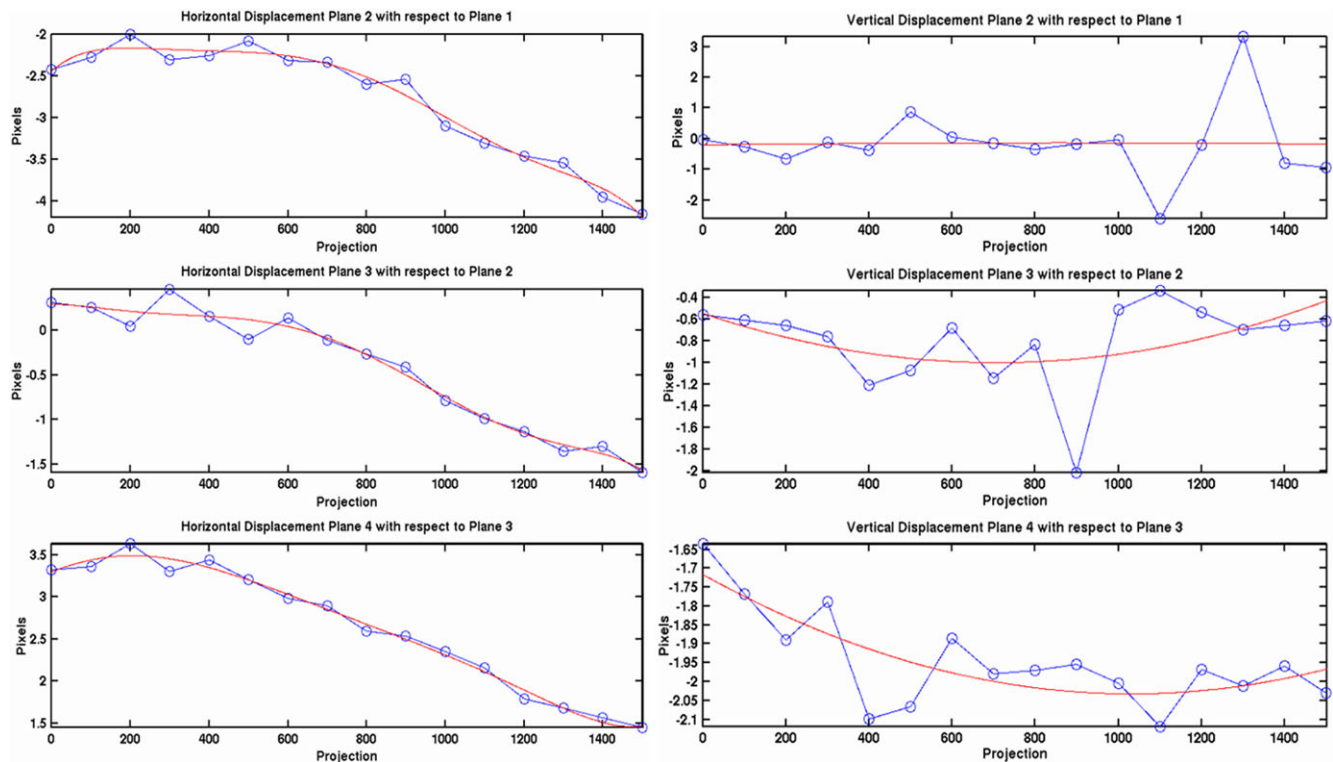

Fig. 2. Example of shifts curves. The projection number is reported on the abscissa, and the shift value (in pixels) on the ordinate. The blue line is drawn from measurements every 100 projections and the red curve corresponds to the polynomial fit. The difference between measurement and fit is less than 1 pixel everywhere, except in the vertical direction in two projection angles (1100 and 1300), indicating the scan was stable and registration successful except in those two points.

Mutual Information method.   As an alternative to the cross-correlation-based method, we evaluated a mutual information (MI)-based registration algorithm. MI is usually employed in multimodality imaging, where the contrast can be different in the two images (Maes *et al.*, 1997; Viola & Wells, 1997). It has the major advantage to be invariant to intensity changes between images, for example inversion contrast. Consider two images *A* and *B*. Their pixels are indexed by *a* and *b*, respectively. The MI index of *A* and *B* is expressed as

$$MI(A, B) = \sum_{a \in A} \sum_{c \in B} p_{AB}(a, b) \log \left(\frac{p_{AB}(a, b)}{p_A(a) p_B(b)} \right), \quad (11)$$

where $p_{AB}(a, b)$ is the joint probability distribution function of *A* and *B*, $p_A(a)$ and $p_B(b)$ the marginal probability distribution functions of *A* and *B*, respectively.

The MI index of two images can be zero or positive; it is equal to 0 if the two images are independent, and increases with the similarity of the two images. In our case, we can have substantially different contrast in the images to be registered, due to strong interference fringes that change as propagation distance changes. The idea behind this method is to assume a mapping between the intensities of the two images without assuming a specific functional mapping (identity, linearity etc.).

We implemented this approach by interfacing *Elastix* (Klein *et al.*, 2010; Shamonin *et al.*, 2013) from GNU Octave. The choice of *Elastix* was based on features such as a variety of different similarity measures, and multiresolution optimisation strategies, which could useful in the case of larger shifts. Because the computation time needed for the registration of each projection angle increases when using more advanced similarity measures, it is advisable to perform the computations in parallel. For example, using current personal computers, registering two 2048 × 2048 images using cross-correlation takes up to 10 s, whereas registration using the MI approach takes up to 5 min. We also included the possibility to take into account rotation and magnification in the image transformations. This allows to correct, for example, for roll in the translation stage, and imprecision or drift of the *z* position of the sample. The latter can be useful if the computed theoretical value of magnification does not accord with the actual magnification of the projections in the case of cone beam tomography.

Quantification of resolution

The loss of resolution in the reconstructed image due to the misalignments was evaluated for random normally distributed shifts with different standard deviations σ. For this purpose, edge profiles of the boundary of the reconstructed sphere phantom were calculated at several positions, always perpendicular to the boundary. In the theoretical case of perfect reconstruction of the underlying phantom volume, the edge profiles should be step functions. Thus one can interpret the measured

edge profile as the edge spread function (ESF) of the imaging system. From the ESF, one can then calculate the line spread function (LSF) by taking the derivative of the ESF (Ahmed, 2015). Here, this was done analytically by fitting the ESF with a sum of error functions, which yields a sum of Gaussians as derivative. The LSF can then be used to determine the system's resolution. We chose the full width at half maximum (FWHM) of the LSF as a measure of the resolution.
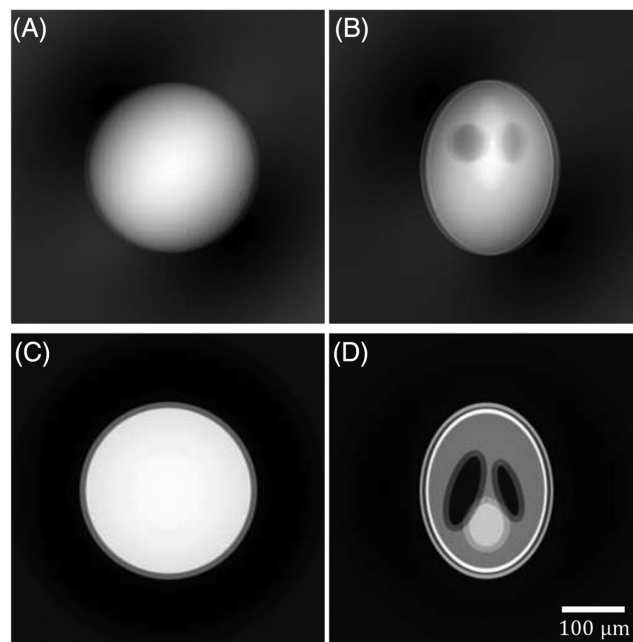

Fig. 3. Phase maps and phase tomograms of two phantoms retrieved from simulated diffraction patterns with a constant shift of 5 pixels in the longest propagation distance. (A) Sphere phantom, (B) modified 3D Shepp–Logan phantom. Note the characteristic doubling of image features, or ghost image, in both images. Note also the presence of low-frequency noise. (C) Reconstructed phase tomographic slice of the sphere and (D) the 3D Shepp-Logan phantom. Also in the object domain we can observe a characteristic doubling of features or ghost image.
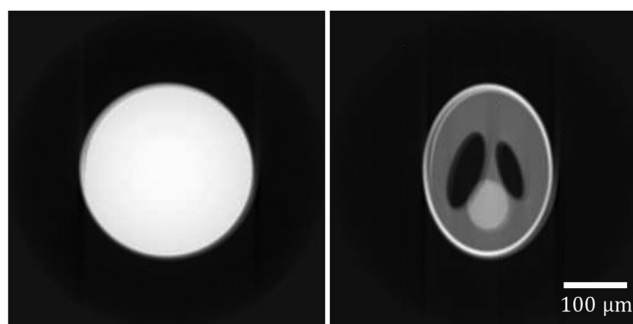

Fig. 4. Reconstructed slices of two different phantoms where a linear drift with a maximal shift of 5 pixels at the last projection angle was applied in the longest propagation distance.
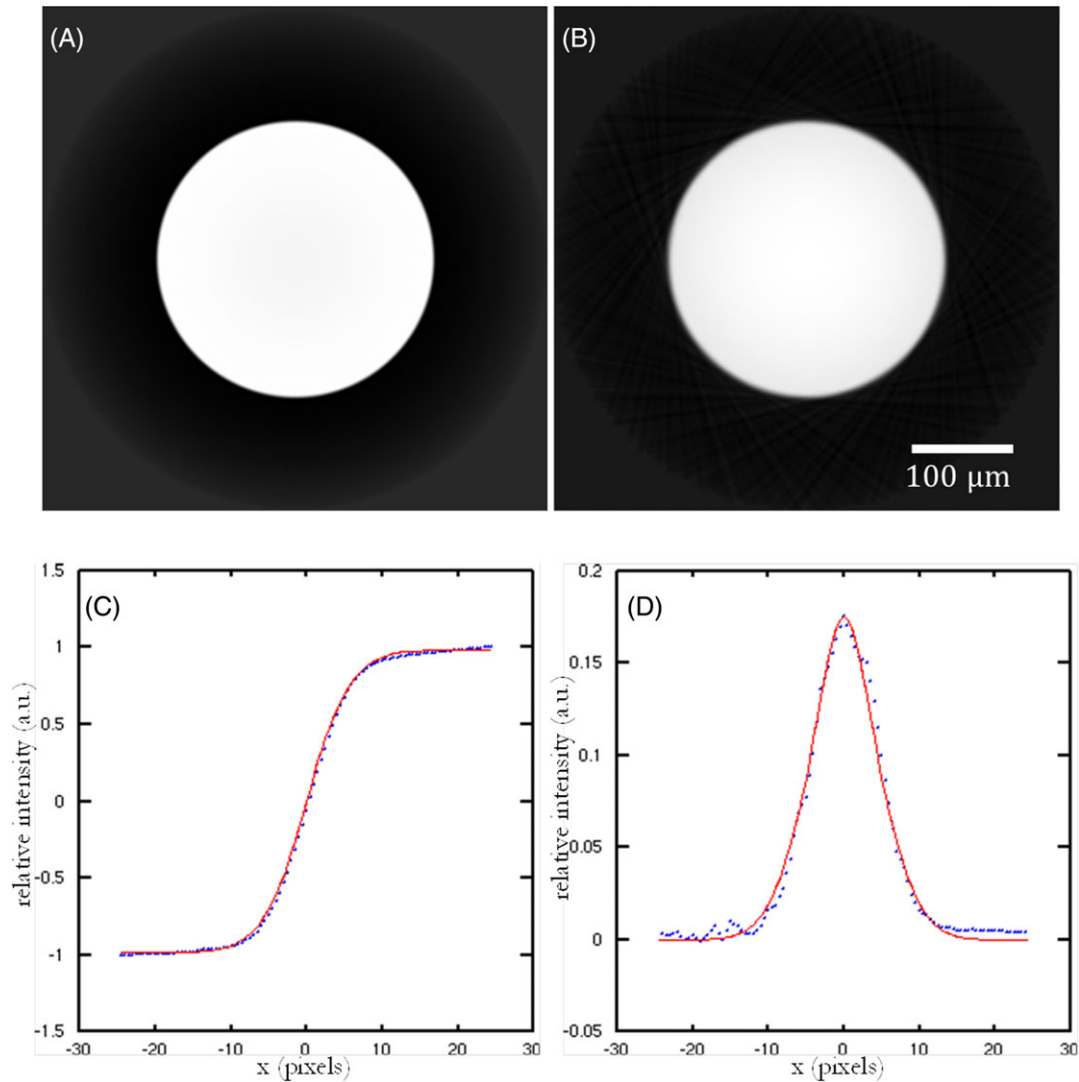
Fig. 5. Reconstruction from phase maps retrieved from (A) nonshifted diffraction patterns, (B) randomly shifted diffraction patterns with a standard deviation of one pixel. (C) ESF and (D) LSF for a random motion with standard deviation $\sigma = 4$. (C) Measured ESF (blue dots) and fit with a sum of error functions (red line). (D) LSF calculated numerically (blue dots) and analytically from fit (red line). The pixel size was defined at 1 μm.
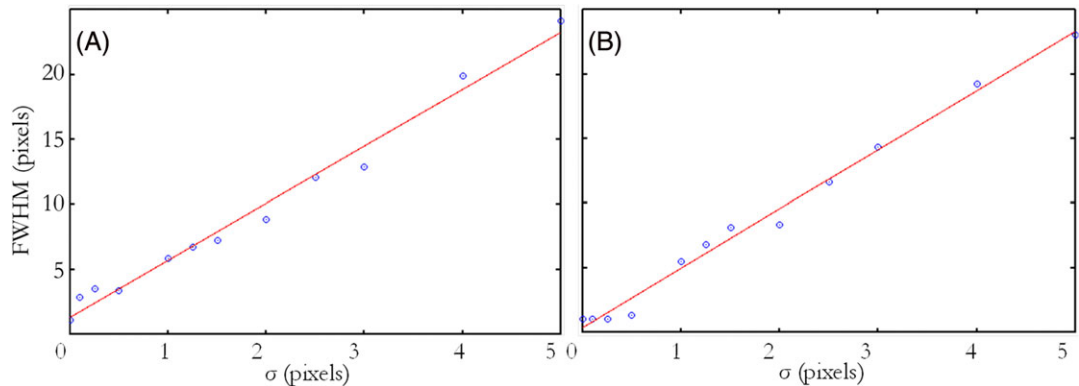

Fig. 6. Full width at half maximum (FWHM) of the line spread function plotted against the standard deviation of the random shifts together with a linear least squares fit of the obtained points for (A) phase tomography and (B) attenuation-based CT. Goodness of fit: (A) $R^2 = 0.98$ and (B) $R^2 = 0.99$. Slope of regression line: (A) $m = 4.38$ and (B) $m = 4.59$. The pixel size was defined at 1 μm.
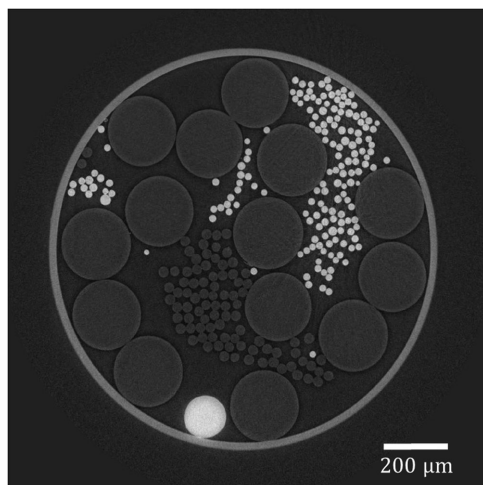
Fig. 7. Reconstructed slice of a phantom object acquired at the ESRF ID19 beamline. Correction for sample drift and registration of projections using cross-correlation were performed.

The goodness of fit of the ESF was evaluated by calculating the coefficient of determinationw

$$R^2 = 1 - \frac{\sum_{j=1}^{N} (r_j - \hat{r}_j)^2}{\sum_{j=1}^{N} (r_j - \bar{r})^2}, \qquad (12)$$

where N is the number of measured points, r_j is the jth measured point, $\hat{r}_j$ is the corresponding point of the fitted function and $\bar{r}$ is the mean of the measured data points.

Results

Simulations

Detector misalignment. We simulated a horizontal shift of 5 pixels of the projections in the longest propagation distance. The remaining propagation distances were left aligned. Figures 3(A) and (B) show the resulting phase maps that were retrieved by using the phase retrieval method described in 'Phase Retrieval and tomographic reconstruction' section for the sphere and the modified 3D Shepp-Logan phantom, respectively. Note that no registration ('Cross-correlation-based method' and 'Mutual Information method' sections) was performed here, because the aim is to simulate artefacts arising from misaligment. For both phantoms we can observe a doubling of structures or a ghost image in the direction where the shift was applied. Further, both phase maps are subject to low-frequency noise. This indicates that poor alignment of phase-contrast images could contribute to low-frequency noise in the retrieved phase. The regularisation parameter in the phase retrieval was chosen to minimise this noise by visual evaluation. In Figures 3(C) and (D), the corresponding phase tomograms are shown. Also here a characteristic doubling of features, or ghost image, can be seen. It can be noted that this artefact is similar to the one arising from a poorly adjusted

rotation axis in standard tomography. It could therefore be confounded with this error source in practice.

Sample drift. To investigate the effect of linear drift of the sample during the data acquisition, a continuously increasing shift was applied to the projections of the longest propagation distance. The maximum shift was reached in the last projection angle, at a little bit less than 360°. The projections in the remaining distances were left unchanged. Phase maps were retrieved using the method in 'General scheme' section, without applying any registration, as in 'Detector misalignment' section. Figure 4 shows the resulting tomographic reconstruction for a horizontal drift with a maximal shift of 5 pixels. In the reconstruction, the drift results in blur and a characteristic spiral-shaped artefact.

Vibration. Normally distributed horizontal and vertical shifts with zero mean and a range of different standard deviations were applied on all projections in all propagation distances to model vibration during the data acquisition. Phase maps were retrieved using the method in 'General scheme' section, without applying any registration, as before ('Detector misalignment' section). Figure 5(B) shows the reconstruction with application of random shifts with a standard deviation of one pixel. For comparison, the reconstruction when no motion is applied is also shown in Figure 5(A). As one might expect, the random shift leads to a blurring of the object.

The loss in resolution in the reconstruction was evaluated for different standard deviations σ of the random shifts as described in 'Motion' Section. Figure 5(C) shows the edge spread function (ESF) and a fit for shifts with a standard deviation of $\sigma = 4$, as well as the numerical and analytical derivative (Fig. 5D), that is the line spread function (LSF). For each of the different standard deviations ranging between zero and five, the coefficient of determination was $R^2 > 0.99$. Figure 6(A) shows a plot of the calculated FWHM of the LSF against the standard deviation. A linear fit was calculated with a coefficient of determination $R^2 = 0.98$ and a slope of $m = 4.38$.

For comparison, the calculation of the FWHM of the LSF was also carried out in the case of attenuation-based CT. In this case, random shifts were applied to the nonpropagated projections which were then reconstructed. Surprisingly, the FWHM in the case of phase tomography and attenuation-based CT are very similar, whereas a larger FWHM would have been expected in the phase tomography case, because shifts were applied to all projections of all propagation planes. Further, one could expect misalignments would introduce more artefacts in the phase tomography case due to the subsequent phase retrieval.

Comparison with experimental data. Projection data of the phantom in 'Wire phantom phase μCT' section was reconstructed, a slice is shown in Figure 7. Correction for motion including sample drift and registration of corresponding

projections at different propagation distances using the correlation-based approach (as described in 'Phase Retrieval and tomographic reconstruction' section) were performed. The phase was retrieved using the mixed approach with a homogeneous object prior (Guigay *et al.* 2007; Langer *et al.*, 2010). The regularisation parameter in the phase retrieval was chosen with the L-curve criterion.

For comparison with the artefacts found in our simulations, we repeated the reconstruction of the phantom several times, omitting different steps in the motion correction procedure to emulate a failed registration. A detail of the resulting reconstructions is shown in Figure 8, where (A) corresponds to the reconstruction from Figure 7. First, we omitted the registration but corrected for sample drift, and the distances were roughly aligned by registering the projections of the first projection angle only and applying the same shift to all projection angles (Fig. 8B). Then, we omitted the registration as well as the rough alignment of the planes. The resulting reconstruction is shown in Figure 8(C). Last, we also omitted the sample drift correction, performing no motion correction at all. Some of the arising artefacts are indicated by arrows. The artefacts we observed for constant shifts (Fig. 3) are visible in Figures 8(B) and (C). Both constant shift and motor drift artefacts are visible in Figure 8(D). Comparing the different subfigures we see that most of the artefacts arise when we do not perform the rough alignment of the different projection planes. This suggests that the principal motion in this particular measurement might be due to a slightly misaligned detector translation stage. In contrast to the rough alignment, the registration of every 100th projection does not have a
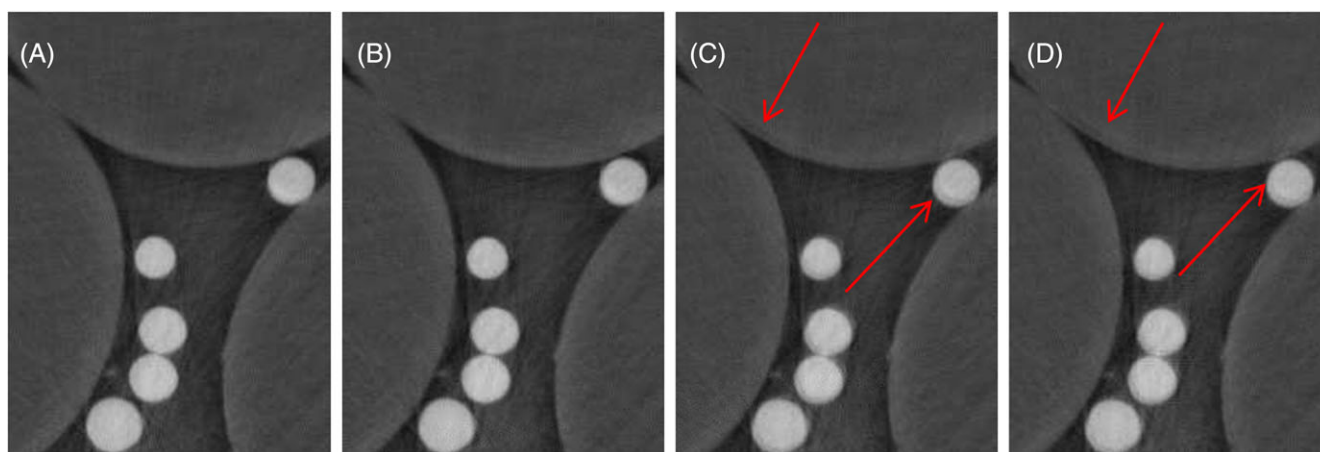

Fig. 8. 150 × 200 μm crops of reconstructions from projection data acquired at the European Synchrotron Radiation Facility, showing the different steps in the motion correction procedure. (A) Correction for sample drift and registration of every 100th projection followed by a fit of shifts. (B) Correction for sample drift and rough alignment by registering the first projection only. (C) Correction for sample drift but no rough alignment of the planes, no registration. Artefacts are indicated by arrows. (D) No preprocessing for motion correction, neither sample drift nor registration of projections. Artefacts are indicated by arrows.
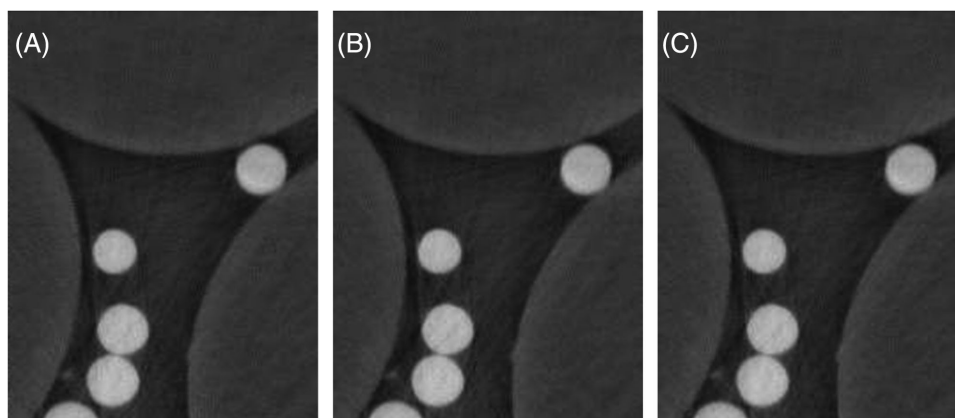

Fig. 9. 150 × 200 μm crops of reconstructions where the registration step was carried out using different approaches: (A) correlation-based registration, (B) normalised cross correlation, (C) normalised mutual information. Quality of reconstruction is not strongly affected, indicating that the three algorithms yielded acceptable results in this case.
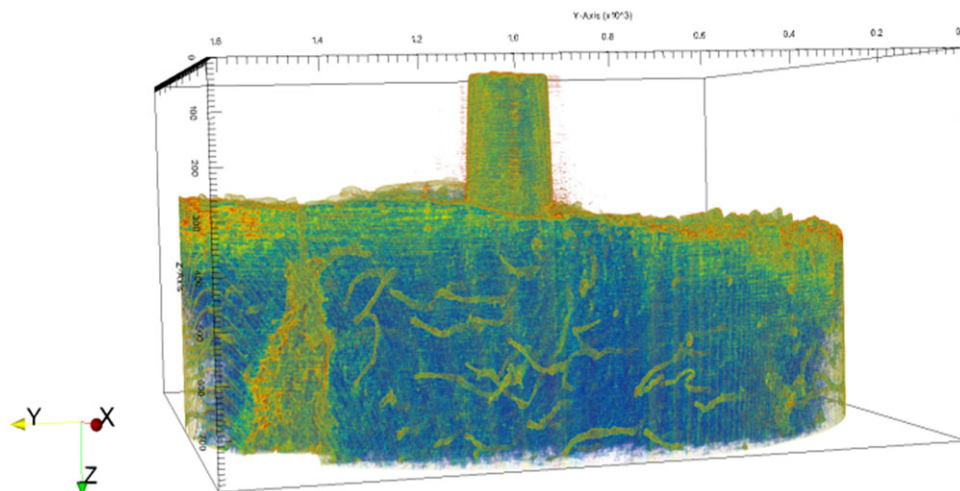
Fig. 10. Volume rendering of a micropillar sample. The box is 51 μm (X) by 51 μm (Y) by 19.9 μm (Z). A lacuna and canaliculi are visible in the base of the sample.
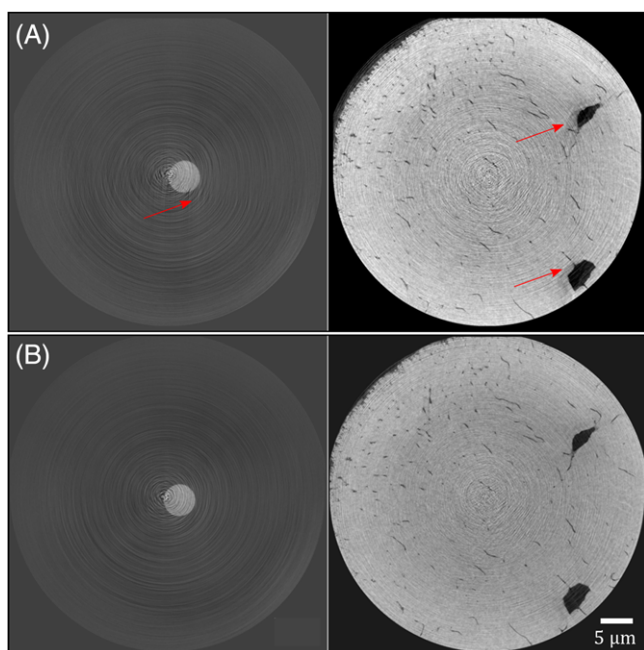

Fig. 11. Example of phase δ_n volume after registering the projections using (A) a correlation-based method; (B) the MI-based method. The left column shows a slice in the micropillar part, and the right column a slice in the base of the micropillar, made of bone. The red arrows highlight typical misalignments artefacts.

visible impact on the reconstruction quality, which suggests remaining motion after motion correction is small in this case.

Mutual information for registration of Fresnel diffraction patterns on experimental data

Wire phantom phase μCT.   We applied three registration algorithms on the phantom data in Figure 7: a registration method based on cross-correlation, normalised mutual information, and normalised cross-correlation, respectively. In this data set, the shifts between the projections are quite small; therefore, the correlation-based local search that was mentioned in 'Phase Retrieval and tomographic reconstruction' section should yield good results and is used as a reference. Figure 9 shows a detail of the reconstruction for the different registration methods. If we examine the resulting phase maps and tomographic reconstructions, it is not obvious which approach gives the most correct registration and thus the best reconstruction. This is the expected outcome because the shifts are small, the propagation distance was relatively small and no particular optics were used so that the contrast was quite similar between the different distances.

Bone micropillar phase nanotomography.   To show the global morphology of the sample, a 3D rendering of the whole scanned volume is shown in Figure 10. The micropillar is seen on top of a larger base.

We compared the classical correlation-based method and the registration method using MI on this sample. The results are shown in Figure 11, for two different vertical positions in the sample. In this case, the MI-based algorithm performs better than the correlation-based one. On the slices reconstructed with the correlation-based approach misalignment artefacts are clearly visible (Fig. 11A), as opposed to the slices reconstructed using the MI-based algorithm where image quality is substantially improved (Fig. 11B).

Discussion and conclusion

We investigated the impact of misalignment of in-line phase-contrast images on the resulting phase tomography images. Different kinds of motion during the data acquisition were

simulated on synthetic data. We showed that the misalignment of the projections of different propagation distances at a given projection angle results in a particular doubling of structure artefact both in the retrieved phase map and the phase tomogram. The artefact somewhat resembles the artefact observed in attenuation-based CT for a poorly chosen rotation axis and could be confused for this. A linear drift of the sample yielded a characteristic spiral shaped artefact. In the case of vibrations, which were modelled using normally distributed random shifts of the phase-contrast images, we observed a blurring of the reconstruction. A sensitivity analysis showed a linear dependence between the system resolution and the standard deviation of the vibration. Moreover, the magnitude of the blur is comparable to the case of vibration in attenuation-based CT. Hence, in-line phase tomography using several distances is not more sensitive to vibrations than attenuation or single-distance phase imaging.

Comparison of the simulated artefacts with real data acquired at the ESRF ID19 beamline on a constructed phantom showed the same types of artefacts mentioned above, and suggests the presence of shifts of the detector (due to a misaligned camera translation stage) and sample drift (due to motor instabilities) in the measurement setup. However, the drift does not necessarily need to be linear as assumed in our simulations. Because the drift and shift were rather small, the improvement in image quality that we achieved by additionally registering the projections of different propagation distances at every 100th projection angle was rather small. Finally, when comparing different registration approaches, based on cross-correlation, normalised cross-correlation and mutual information, the quality of the reconstruction was not greatly improved. This was due to relatively weak defocusing conditions (hence, contrast at the different propagation distances remain quite similar), absence of strong periodic artefacts in the phase-contrast images, and the relatively small shifts.

Applying the mutual information-based method on nanotomography data acquired at the ESRF ID16A beamline, however, yielded substantial improvements. This data shows strong periodical artefacts, and the contrast changes substantially between the imaging planes. This causes cross-correlation-based methods to fail because the hypothesis of linearly dependent contrast between the images is violated. The periodic artefact also creates a strong local optimum in the cross-correlation. The images could be registered using the mutual information-based approach, however. This is probably due to no underlying hypothesis on the contrast in the images (mutual information is actually often used in registration of images from different imaging modalities), as well as a lower sensitivity to periodic structures.

In conclusion, registration of phase-contrast images seems to be a crucial step in obtaining high-quality reconstructions of the phase and consequently the refractive index decrement. This problem is scarcely mentioned in literature, however.

We showed that selection of a registration algorithm that fits the characteristic of the phase-contrast images is necessary for the registration to be robust to the changing contrast and the types of image artefacts encountered. These results should improve the rate of successful reconstructions in in-line phase nanotomography, and reduce operator time for manual registration when correlation-based registration algorithms fail.

Acknowledgements

References

Ahmed, S.N. (2015). *Physics and engineering of radiation detection.* Elsevier, Netherlands. https://doi.org/10.1016/B978-0-12-801363-2.00001-2

Boistel, R., Aubin, T., Cloetens, P. *et al.* (2011). Whispering to the deaf: communication by a frog without external vocal sac or tympanum in noisy environments. *Plos One* **6**, e22080.

Cloetens, P., Ludwig, W., Baruchel, J., Van Dyck, D., Van Landuyt, J., Guigay, J.P. & Schlenker, M. (1999). Holotomography: quantitative phase tomography with micrometer resolution using hard synchrotron radiation x rays. *Appl. Phys. Lett.* **75**, 2912. https://doi.org/10.1063/1.125225

Cloetens, P., Ludwig, W., Boller, E., Peyrin, F., Chlenker, M. & Baruchel, J. (2002). 3D imaging using coherent synchrotron radiation. *Image Anal. Stereol.* **21**(4), S75–S85.

Cloetens, P., Pateyron-Salomé, M., Buffière, J.Y., Peix, G., Baruchel, J., Peyrin, F. & Schlenker, M. (1997). Observation of microstructure and damage in materials by phase sensitive radiography and tomography. *J. Appl. Phys.* **81**, 5878. https://doi.org/10.1063/1.364374

Frachon, T., Weber, L., Hesse, B. *et al.* (2015). Dose fractionation in synchrotron radiation x-ray phase micro-tomography. *Phys. Med. Biol.* **60**, 7543–7566.

Gbur, G. & Wolf, E. (2002). Diffraction tomography without phase information. *Opt. Lett.* **27**(21), 1890–1892.

Goodman, J.W. (2005). *Introduction to Fourier Optics.* Roberts and Company Publishers, New York.

Guigay, J.-P. (1977). Fourier transform analysis of fresnel diffraction patterns and in-line holograms. *Optik* **49**, 121–125.

Guigay, J.P., Langer, M., Boistel, R. & Cloetens, P. (2007). Mixed contrast transfer and transport of intensity approach for phase retrieval in the Fresnel region. *Opt. Lett.* **32**, 1617–1619.

Herman, G.T. (2009). *Fundamentals of Computerized Tomography.* Springer London, London. https://doi.org/10.1007/978-1-84628-723-7

Horng, A., Brun, E., Mittone, A. *et al.* (2014). Cartilage and soft tissue imaging using X-rays: Propagation-based phase-contrast computed

tomography of the human knee in comparison with clinical imaging techniques and histology. *Invest. Radiol.* **49**, 627–34.

Klein, S., Staring, M., Murphy, K., Viergever, M.A. & Pluim, J.P.W. (2010). Elastix: a toolbox for intensity-based medical image registration. *IEEE Transact. Med. Imag.* **29**, 196–205.

Langer, M., Cloetens, P., Guigay, J.-P. & Peyrin, F. (2008). Quantitative comparison of direct phase retrieval algorithms in in-line phase tomography. *Med. Phys.* **35**, 4556–4566.

Langer, M., Cloetens, P., Hesse, B., Suhonen, H., Pacureanu, A., Raum, K. & Peyrin, F. (2014). Priors for X-ray in-line phase tomography of heterogeneous objects. *Philos. Transact. R. Soc. A* **372**, 1–9.

Langer, M., Cloetens, P., Pacureanu, A. & Peyrin, F. (2012a). X-ray in-line phase tomography of multimaterial objects. *Optics Lett.* **37**, 2151–2153.

Langer, M., Cloetens, P. & Peyrin, F. (2010). Regularization of phase retrieval with phase-attenuation duality prior for 3-D holotomography. *IEEE Transact. Image Process.* **19**, 2428–2436.

Langer, M., Pacureanu, A., Suhonen, H., Grimal, Q., Cloetens, P. & Peyrin, F. (2012b). X-ray phase nanotomography resolves the 3D human bone ultrastructure. *Plos One* **7**, e35691. https://doi.org/10.1371/journal.pone.0035691

Maes, F., Collignon, A., Vandermeulen, D., Marchal, G. & Suetens, P. (1997). Multimodality image registration by maximization of mutual information. *IEEE Transact. Med. Imag.* **16**, 187–198.

Mirone, A., Gouillart, E., Brun, E., Tafforeau, P. & Kieffer, J. (2013). PyHST2: an hybrid distributed code for high speed tomographic reconstruction with iterative reconstruction and a priori knowledge capabilities. *NIMA B* **324**, 41–48.

Momose, A. & Fukuda, J. (1995). Phase-contrast radiographs of nonstained rat cerebellar specimen. *Med. Phys.* **22**, 375–379.

Nugent, K., Gureyev, T., Cookson, D., Paganin, D. & Barnea, Z. (1996). Quantitative phase imaging using hard X Rays. *Phys. Rev. Lett.* **77**, 2961–2964.

Op de Beeck, M., Van Dyck, D. & Coene, W. (1996). Wave function reconstruction in HRTEM: the parabola method. *Ultramicroscopy* **64**, 167–183.

Paganin, D., Mayo, S.C., Gureyev, T.E., Miller, P.R. & Wilkins, S.W. (2002). Simultaneous phase and amplitude extraction from a single defocused image of a homogeneous object. *J. Microsc.* **206**, 33–40.

Rit, S., Vila Oliva, M., Brousmiche, S. *et al.* (2014). The reconstruction toolkit (RTK), an open-source cone-beam CT reconstruction toolkit based on the insight toolkit (ITK). *J. Phys.: Conf. Ser.* **489**, 12079. https://doi.org/10.1088/1742-6596/489/1/012079

Schwiedrzik, J., Raghavan, R., Bürki, A., LeNader, V., Wolfram, U., Michler, J. & Zysset, P. (2014). In situ micropillar compression reveals superior strength and ductility but an absence of damage in lamellar bone. *Nat. Mater.* **13**, 740–747.

Shamonin, D.P., Bron, E.E., Lelieveldt, B.P.F., Smits, M., Klein, S., Staring, M. & Alzheimer's Disease Neuroimaging Initiative. (2013). Fast parallel image registration on CPU and GPU for diagnostic classification of Alzheimer's disease. *Front. Neuroinform.* **7**, 50. https://doi.org/10.3389/fninf.2013.00050

Snigirev, A., Snigireva, I., Kohn, V., Kuznetsov, S. & Schelokov, I. (1995). On the possibilities of x-ray phase contrast microimaging by coherent high-energy synchrotron radiation. *Rev. Sci. Instr.* **66**, 5486. https://doi.org/10.1063/1.1146073

Teague, M.R. (1982). Irradiance moments: their propagation and use for unique retrieval of phase. *J. Opt. Soc. Am.* **72**, 1199. https://doi.org/10.1364/JOSA.72.001199

Villanova, J., Cloetens, P., Suhonen, H. *et al.* (2014). Multi-scale 3D imaging of absorbing porous materials for solid oxide fuel cells. *J. Mater. Sci.* **49**, 5626–5634.

Viola, P. & Wells III, W.M. (1997). Alignment by maximization of mutual information. *Int. J. Comp. Vis.* **24**, 137–154.

Zabler, S., Cloetens, P., Guigay, J.-P., Baruchel, J. & Schlenker, M. (2005). Optimization of phase contrast imaging using hard x rays. *Rev. Sci. Instr.* **76**, 73705. https://doi.org/10.1063/1.1960797

Zanette, I., Daghfous, G., Weitkamp, T. *et al.* (2013). Looking inside marine organisms with MRI and X-ray tomography. *Imaging Marine Life* (ed. by E.G. Reynaud). Wiley-VCH Verlag GmbH & Co. KGaA, Weinheim, Germany. https://doi.org/10.1002/9783527675418.ch

Zanette, I., Weitkamp, T., Lang, S., Langer, M., Mohr, J., David, C. & Baruchel, J. (2011). Quantitative phase and absorption tomography with an X-ray grating interferometer and synchrotron radiation. *Phys. Status Solidi A* **208**, 2526–2532.